Photo-irradiation synthesis of Fe_3O_4 and GO/Fe_3O_4 magnetic nanoparticles for tartrazine adsorption: a comparative and reuse studies

Ruba Fahmi Abbas*, Mohammed Jasim M. Hassan, Ahmed Mahdi Rheima

Chemistry Department, College of Science, Mustansiriyah University, Baghdad, Iraq, emails: rubaf1983@uomustansiriyah.edu.iq (R.F. Abbas), dr.moh2004@uomustansiriyah.edu.iq (M.J.M. Hassan), ahmed.rheima@yahoo.com (A.M. Rheima)

ABSTRACT

In this study, the adsorption of tartrazine (E102) dye on the surface of ferrous ferric oxide (magnetite) (Fe_3O_4 MNPs) and graphene oxide nano-sheets/ferrous ferric oxide (GO/Fe_3O_4 MNPs) as adsorbents was examined. The photo-irradiation method was successfully used to synthesize Fe_3O_4 MNPs and GO/Fe_3O_4 MNPs using UV light. Raman spectroscopy was employed to characterize the GO and GO/Fe_3O_4 MNPs. X-ray diffraction analysis, field-emission scanning electron microscopy, and energy-dispersive X-ray spectroscopy were utilized to characterize the Fe_3O_4 MNPs and GO/Fe_3O_4 MNPs. Optimal adsorption conditions were studied, including a contact time of 60 min, an MNPs amount of 0.05 g, pH 2, tartrazine dye concentration of 20 mg/L, and a temperature of 318 K. Langmuir, Freundlich, and Dubinin–Radushkevich isotherm models were employed to fit the experimental equilibrium data at five different temperatures (288, 298, 308, 318, and 328 K). It was noticed that tartrazine adsorption on Fe_3O_4 MNPs and GO/Fe_3O_4 MNPs is consistent with the Langmuir model at 313 K but not with the Freundlich or Dubinin–Radushkevich model. The separation factor (R_L) values ranged between 0 and 1, confirming that the adsorption of tartrazine onto Fe_3O_4 MNPs and GO/Fe_3O_4 MNPs was favorable at different temperatures. The pseudo-second-order rate kinetics suggests that both MNPs are promising materials for the removal of tartrazine dye from aqueous solutions. Thermodynamic studies showed that the adsorption processes are endothermic, non-spontaneous, and an increase in order at the interface for both MNPs surfaces. All the results confirm that Fe_3O_4 MNPs and GO/Fe_3O_4 MNPs have the potential to be efficient, low-cost, reusability, and stable adsorbents for the removal of tartrazine dye from aqueous solutions.

Keywords: Tartrazine; Photo-irradiation; Adsorption; Graphene oxide nano-sheets/ferrous ferric oxide (GO/Fe_3O_4 MNPs); Raman spectroscopy; Dubinin–Radushkevich

1. Introduction

Synthetic dyes offer numerous advantages over natural dyes. They provide light fastness, maintain vibrancy, and resist fading easily, even with prolonged exposure to sunlight. These dyes are vivid and offer an extensive array of color options. They exhibit resistance to changes in pH, temperature, and chemicals [1]. Furthermore, synthetic dyes can be seamlessly integrated into diverse materials, and they are compatible with various manufacturing processes, including printing, dyeing, and coating [2]. Tartrazine (E102) finds widespread usage as a food colorant, imparting a yellow or orange hue to various foods and beverages. It serves as a food additive, with its permissible concentrations being stringently regulated [3]. Indeed, studies have indicated that tartrazine (TZ) and other azo dyes can have several detrimental effects on human health. These include conditions such as asthma, hyperactivity, urticaria, migraines, and angioedema. Moreover, there is a potential association with mutagenic tendencies, along with a suggested link to thyroid cancer [4]. Consequently, treating wastewater containing TZ and other azo dyes before discharge becomes pivotal

* Corresponding author.

in mitigating their environmental impact. Various methods have been employed to address TZ in aqueous solutions, such as utilizing photocatalytic reusable TiO_2/PVDF-TrFE membranes (TiO_2/PVDF-TrFE membranes) [5], photocatalytic nanocomposite polymer-TiO_2 membranes [6], advanced oxidation processes like electrochemical and sonochemical treatment employing boron-doped diamond (BDD) electrodes [7], as well as adsorption and catalytic degradation through Fe-modified zeolite [8]. Additionally, advanced oxidation processes involving ultraviolet light-emitting diodes (UV LEDs) coupled with hydrogen peroxide have been utilized [9]. Furthermore, treatments encompass heterogeneous photocatalysis employing ZnO photocatalyst in batch reactors [10], photocatalytic degradation using TiO_2 and UV light [11], and microwave-enhanced UV/H_2O_2 degradation [12]. Adsorption has consistently proven to be an efficacious technique for treating TZ containing wastewater. Utilizing adsorption for azo dye treatment offers numerous advantages, including its simplicity, cost-effectiveness, high removal efficiency, generation of non-toxic by-products, utilization of readily available materials, and compatibility with various instruments [13]. A variety of adsorbents have been employed for the elimination of TZ from aqueous solutions, such as activated carbon [14,15], biochar [16,17], and clay minerals [13,18]. Magnetic nanotechnology is widely recognized as a highly promising field with numerous potential applications [19]. Furthermore, the utilization of magnetic nanomaterials (MNs) for dye adsorption has demonstrated significant advantages. These include selective adsorption or binding to target analytes, a high adsorption capacity ensuring efficient removal of the target substances, facile separation from the system using an external magnetic field without the need for filter papers or centrifugation, and the ability to recover and reuse MNPs multiple times, making them both cost-effective and environmentally friendly [20]. In this paper, we present the synthesis of Fe_3O_4 MNPs and graphene oxide nano-sheets/ferrous ferric oxide (GO/Fe_3O_4 MNPs) through a photo-irradiation method. The photo-irradiation method offers several advantages, including a very simple, environmentally friendly, scalable, and straightforward method. Moreover, UV light can quickly and effectively initiate the synthesis of both Fe_3O_4 MNPs and GO/Fe_3O_4 MNPs. The size, morphology, and composition of the MNPs can be controlled by varying the photo-irradiation conditions. On the other hand, the incorporation of graphene oxide (GO) is driven by its capability to form exceptionally stable nanocomposites with improved performance, easily obtaining a well-crystallized material. The features of Fe_3O_4 MNPs and GO/Fe_3O_4 MNPs include high selectivity and sensitivity due to the large surface area and high adsorption capacity. This method is fast, eco-friendly, and cost-effective as the adsorption method can be easily recycled and reused by both MNPs [21,22]. The surface properties of Fe_3O_4 MNPs and GO/Fe_3O_4 MNPs were evaluated using characterization methods including X-ray diffraction (XRD), energy-dispersive X-ray spectroscopy (EDX), mapping, and field-emission scanning electron microscopy (FESEM). The study revolves around investigating the adsorption traits of tartrazine (TZ) dye for its removal from aqueous solutions. Furthermore, in an effort to comprehend the adsorption mechanism, the impacts of diverse parameters and the equilibrium isotherm, thermodynamics, and kinetics dosing for adsorption were documented and discussed.

2. Materials and methods

2.1. Chemicals

Graphite native (B.D.H), iron(III) ammonium sulfate ($NH_4Fe(SO_4)_2 \cdot 12H_2O$) (≥99.0%), ammonium iron(II) sulphate hexahydrate (($NH_4)_2Fe(SO_4)_2 \cdot 6H_2O$) (≥99.0%), sodium hydroxide (NaOH) (≥97.0%), HCl (37%), urea (NH_2CONH_2) (≥99.0%), and tartrazine (95%). All aqueous solutions and dispersions were prepared using de-ionized water (DW).

2.2. Instruments

Different types of instruments were used in this study: a water bath (BS11 Digital, JEIO Korea, TECH), a UV-Vis Spectrophotometer (Single Beam, Model No. HV-295, India), an energy-dispersive X-ray analyzer (EDX) (JEOL JSM6510 LV, Japan), a Raman Spectrophotometer (PerkinElmer, Lambda 25 Spectrophotometer, USA), a FESEM (JEOL JSM-6510 LV, Japan), and an X-ray diffraction analyzer (Philips PW1730, USA).The characterization and evaluation of surface properties of MNPs were done at Beam Gostar Taban Company in Tehran, Iran.

2.3. Methods

2.3.1. Synthesis of graphene oxide

Synthesis of GO nano-sheets was achieved by using the modified Hummers method [23]. 2 g of graphite powder and 1 g of $NaNO_3$ were mixed with 150 mL of 98% H_2SO_4. This mixture was placed in an ice bath to maintain a temperature below 5°C and stirred for 30 min. After that, 8 g of $KMnO_4$ was slowly added to the mixture and kept under a magnetic stirrer for 6 h. 1 L of distilled water (DW) was added, followed by the addition of 20 mL of 32% H_2O_2 to stop the reaction, with intense stirring. Finally, the product was cleaned and immersed in DW and a 20% HCl solution using several steps. The black-brown product was dried at room temperature overnight to obtain graphene oxide nano-sheets.

2.3.2. Synthesis of MNPs

Photo-irradiation method components are:

- UV source with maximum intensity at a wavelength of 365 nm (125 W mercury medium pressure lamp).
- A quartz tube is used as a jacket to immerse the UV source in the solution. Quartz is often used because it withstands the high temperatures generated by the lamp and can be transparent to UV light.
- Pyrex tube is used as a reactor.
- Ice bath is important to control the reaction temperature, prevent unwanted side reactions, and cool the reactor [24].

0.15 g of GO nano-sheets was dispersed in 30 mL of de-ionized water for 30 min (solution A). 30 mL of 0.02 mol $NH_4Fe(SO_4)_2 \cdot 12H_2O$ (solution B) was stirred for

30 min and after that, it was mixed with 30 mL of 0.01 mol $(NH_4)_2SO_4 \cdot FeSO_4 \cdot H_2O$ under a magnetic stirrer for 30 min (solution C). Then, 40 mL of 0.01 mol NH_2CONH_2 is gradually added to the solution from the burette (drop by drop). After that, solution C and solution A were mixed under a magnetic stirrer for 30 min. The mixture was irradiated by photocell for 30 min. The temperature was kept under 5°C by using an ice bath. For precipitation of MNPs, add 100 mL of 6 M NaOH by using dropper under a magnetic stirrer until black precipitate appears and let it stirrer for 30 min. The MNPs precipitate is separated and cleaned with DW numerous times through a decantation process. The precipitate is then dried at 60°C for a few days. To prepare Fe_3O_4 MNPs, repeat all the steps without adding GO nano-sheets (solution A) (Fig. 1).

2.3.3. Adsorption studies

Five factors were investigated, namely: contact time (15–90 min), a specific amount of MNPs (0.01–0.15 g), pH (2–10), concentration of TZ dye (20–40 mg/L), and temperature (288–328 K). The pH of TZ dye solutions was adjusted using NaOH and HCl (0.01 M). The calibration curve of TZ dye showed a maximum absorbance at λ_{max} of 427 nm and a molar absorptivity ($\mathcal{C}$ = 0.039 L/g·cm). Five different temperatures (288–328 K) were tested in the isotherm study. The isotherm study was carried out by adsorbing 20 mg/L TZ dye onto MNPs using a set of tubes containing 10 mL at a contact time of 60 min. The efficiency of adsorbed amount q_e of adsorption of TZ dye and removal% was defined as in Eqs. (1) and (2) [25,26].

$$q_e = \frac{(C_0 - C_e)V}{m} \tag{1}$$

$$\text{Removal \%} = \frac{(C_0 - C_e)}{C_0} \times 100 \tag{2}$$

where C_o and C_e are the initial and final concentrations of TZ dye (mg/L), m is the weight of Fe_3O_4 MNPs and GO/Fe_3O_4 MNPs (g) and V is the volume of TZ dye (L).

3. Results and discussion

3.1. Magnetite nanoparticle characterization

3.1.1. Raman spectroscopy

Raman spectroscopy is used to characterize the chemical and physical properties of carbon materials. The D, G, and 2D peaks observed under Raman spectroscopy are like fingerprints for carbon materials. The D band is considered a defect band, and its intensity is directly related to the level of defects. The G band corresponds to the crystalline structure of the sample and represents the vibrational mode of sp2 hybridized carbon atoms found in graphene sheets. The 2D band is used to determine the thickness of graphene layers and originates from the second-order Raman scattering process [27,28]. The G and D bands in GO are often used to monitor changes during various treatments. In this study, the D band of GO is approximately 1,355 cm⁻¹, while the G band is around 1,589 cm⁻¹ (Fig. 2a). The 2D band appears at a position of 2,685.13 cm⁻¹. Exfoliation, which involves the
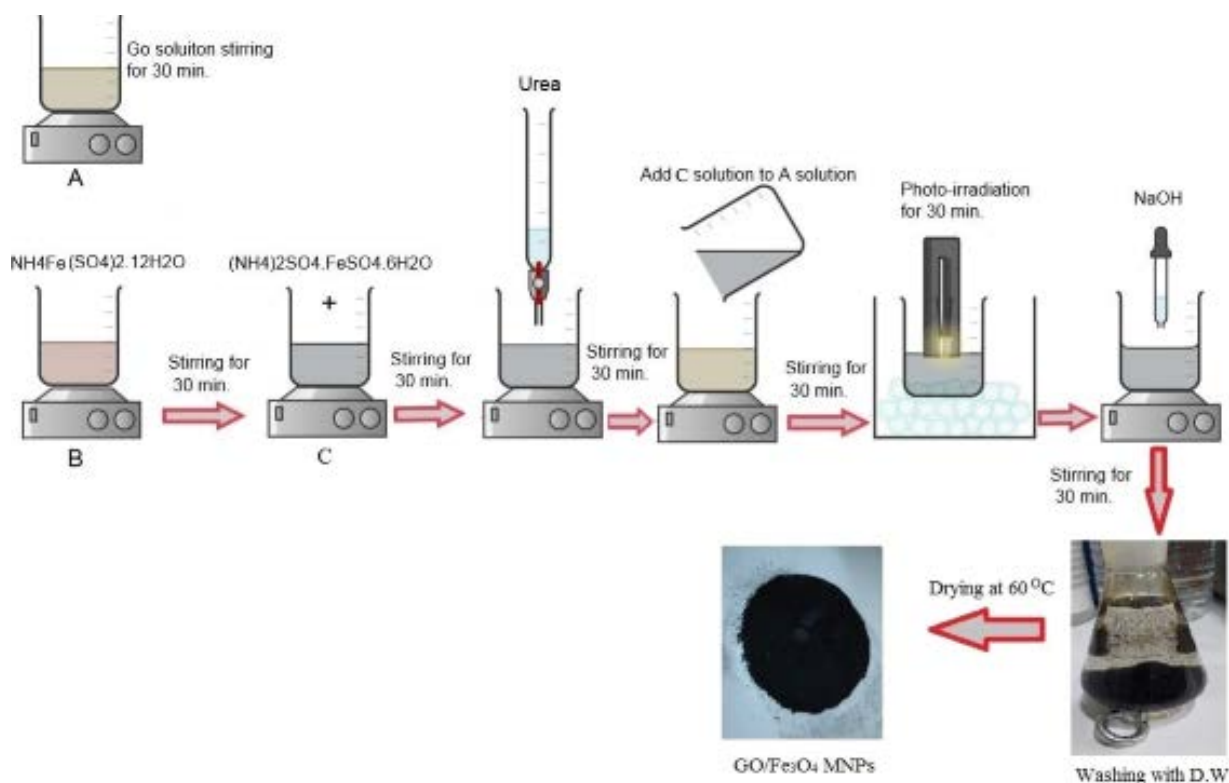

Fig. 1. Scheme of synthesis GO/Fe_3O_4 MNPs using photo-irradiation method.

insertion of oxygen functional groups, disrupts the graphitic order. As a result, the low-intensity ratio of IG/ID is 0.957, indicating exfoliation and a decrease in the number of layers. The ratio of I2D/IG bands for a defect-free (high-quality) single-layer graphene should be equal to 2. In this study, the ratio I2D/IG is measured to be 0.126, which is often used to confirm a defect-free graphene sample (Table 1) [29,30]. The Raman spectra of the GO/Fe$_3$O$_4$ MNPs (graphene oxide/iron oxide magnetic nanoparticles) actually represent a combination of both components, suggesting that no reaction occurred between GO and Fe$_3$O$_4$. They were originally formed during the photo-irradiation method. For GO/Fe$_3$O$_4$ MNPs, the observed shift towards lower intensity in the D, G, and 2D bands compared to GO suggests an increased level of disorder and a higher number of defects in the graphene layers. This shift is likely due to the partial reduction of GO to graphene during the synthesis process of GO/Fe$_3$O$_4$ MNPs. The high-intensity ratio of ID/IG is about 9.01 because of the reduction of GO sheets after Fe$_3$O$_4$ loading on it during the photo-irradiation method. This result is similar to previous studies [31,32]. The ratio I2D/IG value is 1.963 after Fe$_3$O$_4$ loading onto GO, which indicates that I2D/IG bands are for defect-free (high-quality) single-layer graphene (Table 1). Deconvolution aims to separate the original signals from the convoluted signal. Peak deconvolution techniques are widely used to extract information about individual peaks in complex mixtures. In the Raman spectrum, several weak intense modes are usually overlapped with the neighboring prominent modes and cause broadening. Therefore, peak deconvolution was used to extract the contribution of each Raman mode from the broadened Raman peak [33]. In this study, peak analysis fitting of the deconvoluted Raman spectra is shown in Fig. 2b and c.

3.1.2. XRD analysis

It was necessary to combine Fe$_3$O$_4$ nanoparticles (NPs) with graphene oxide in order to obtain nanocomposites with enhanced performance [34]. XRD measurements were used to determine the product's crystalline structure. The
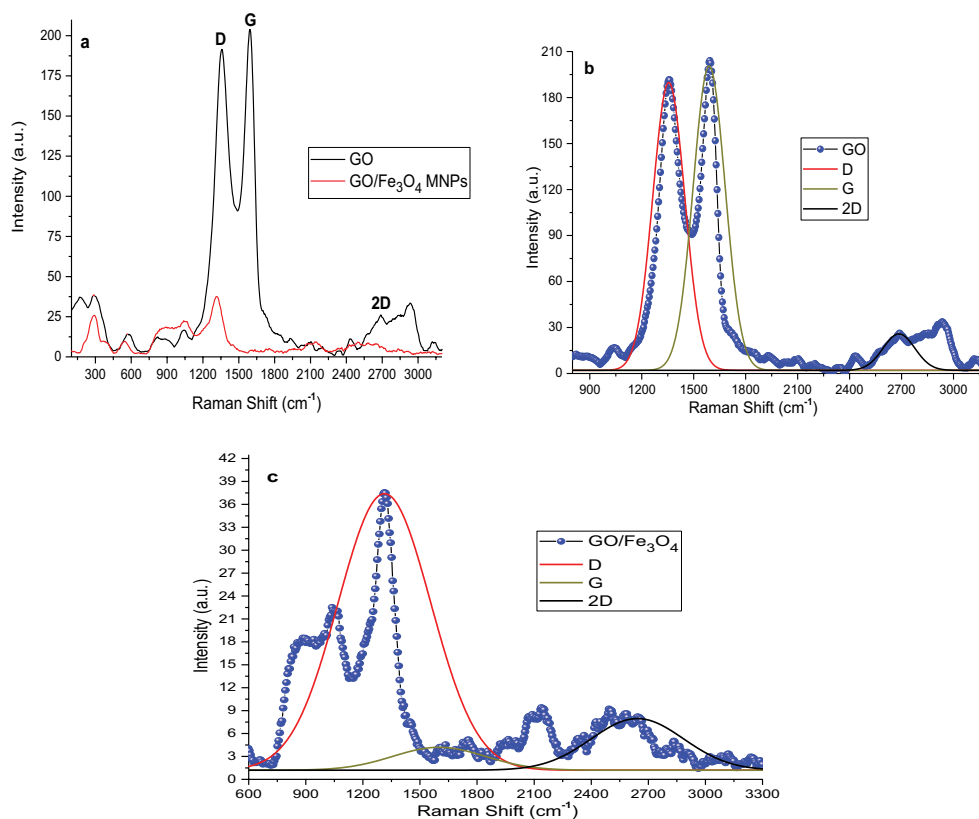

Fig. 2. Raman spectra of GO and GO/Fe$_3$O$_4$ MNPs (a), deconvoluted Raman spectra of GO (b), and GO/Fe$_3$O$_4$ MNPs (c).

Table 1
Positions and relative intensities of D, G, and 2D bands of GO nano-sheet and GO/Fe$_3$O$_4$ MNPs

Sample	D band		G band		2D band		ID/IG	I2D/IG
	Position (cm^{-1})	Intensity	Position (cm^{-1})	Intensity	Position (cm^{-1})	Intensity	Position (cm^{-1})	Intensity
GO nano-sheet	1,355.90	190.33	1,589.14	198.75	2,685.13	25.22	0.957	0.126
GO/Fe$_3$O$_4$ MNPs	1,313.90	37.51	1,602.74	4.16	2,643.54	8.17	9.016	1.963

presence of strong and sharp peaks indicates high crystallinity, while broad peaks suggest small crystallite sizes [35]. A Philips PW1730 diffractometer with Cu Kα radiation (λ = 1.54060 Å) was used for X-ray diffraction (XRD) analysis. During the XRD analysis of graphene oxide (GO), two sharp diffraction peaks were observed. The first peak corresponds to the (001) plane and appears at 2θ = 12.15°, while the second peak corresponds to the (100) plane and appears at 2θ = 42.53° (Figs. 3 and 4d). The (001) peak indicates the presence of interlayer spacing between the GO sheets, which is typically larger than the interlayer spacing in pristine graphene. Moreover, the (100) peak indicates the ordered arrangement of graphene oxide sheets in the (100) plane. The grain size of GO was calculated to be 10.49 nm using the Scherrer equation. Peaks at 2θ = 18.21°, 30.21°, 35.67°, 43.39°, 54.01°, 57.32°, 63.00°, 71.36°, 74.47°, 75.23° and 79.30° correspond to the reflections from the (111), (220), (311), (400), (422), (511), (440), (620),(533), (622), and (444) of Fe$_3$O$_4$ (AMCSD code 0007824) (Fig. 4a and b). While peaks at 2θ = 18.74°, 30.64°, 36.10°, 43.71°, 54.21°, 57.75°, 63.43°, 71.90°, 74.80°, 75.76° and 79.94° are due to X-ray diffraction from the (111), (220), (311), (400), (422), (511), (440), (620),(533), (622), and (444) planes of GO/Fe$_3$O$_4$ in the nanocomposite (Fig. 4c). The crystallite size for Fe$_3$O$_4$ of 11.6 nm and for GO/Fe$_3$O$_4$ MNPs of 12.02 nm was calculated from sharp XRD
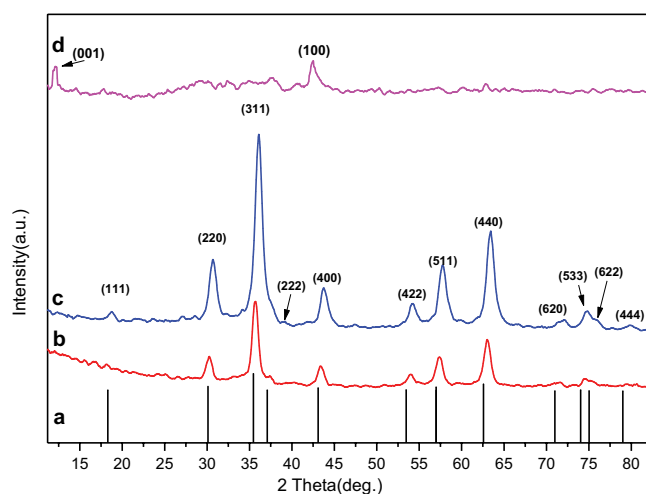
peaks. It is calculated using the standard Debye–Scherrer equation $D = 0.9\lambda/(\beta\cos\theta)$, where D refers to the diameter of the nanoparticles, λ (Cu Kα) = 0.15406 nm, and β represents the full width at half maximum of the diffraction lines.

3.1.3. FESEM observation

FESEM is a well-suited technique for analyzing surface morphology and determining the size and shape of nanoparticles [36]. Fig. 5 shows FESEM images at different magnifications with particle size distribution histogram of Fe$_3$O$_4$ NPs and GO/Fe$_3$O$_4$, respectively. FESEM images at different magnifications of GO nano-sheets showed thin fluffy curtain-like morphology and rich wrinkle-like sheet structure (Fig. 5) [37]. The FESEM images revealed that both Fe$_3$O$_4$ MNPs and GO/Fe$_3$O$_4$ MNPs exhibited a spherical shape. The FESEM images revealed that both Fe$_3$O$_4$ MNPs and GO/Fe$_3$O$_4$ MNPs exhibited a spherical shape (Figs. 6c and 7c). The size distribution of the MNPs was determined and fitted using a Gaussian fit. The nanoparticles exhibited a wide size distribution with an average size of 25.064 and 22.910 nm for Fe$_3$O$_4$ MNPs and GO/Fe$_3$O$_4$ MNPs, respectively (Figs. 6d and 7d).

3.1.4. EDX mapping analysis

EDX is a technique used to analyze the elemental composition of a sample. As can be seen, the high purity peaks of iron, oxygen, and carbon elements in EDX analysis indicate the high purity of the synthesized Fe$_3$O$_4$ MNPs and GO/Fe$_3$O$_4$ MNPs (Figs. 8 and 9). X-ray mapping refers to the process of using X-rays to create spatial maps or images of the distribution of elements or compounds within a sample. As shown in Figs. 10 and 11, the X-ray mapping displays a homogeneous dispersion of Fe, O, and C atoms in the composite.

3.1.5. Selection of wavelength (λ_{max}) for optimal conditions

Light absorption of food dye is pH-dependent since spectral changes of food dyes appear at pH 2 and 12 [38]. The maximum absorbances (λ_{max}) of the TZ dye solution were determined in the different pH ranges (2–12) to study the spectral behavior of TZ dye and to find the optimum pH for the adsorption and desorption process. As shown in Fig. 12, a maximum absorbance appeared at λ_{max} of 427 nm at pH 2, 4, and 7. In the basic medium, the maximum absorbances (λ_{max}) shifted to the lower value of 396 nm at pH 11 and 12.

3.2. Effect study for the adsorption conditions

3.2.1. Effect of contact time

Removal studies of TZ dye have been conducted at different contact times (15, 30, 45, 60, and 90 min). All other parameters were kept constant at (0.05 g, 25 mg/L, pH 7.3, and 298 K). The figure shows that the rate of TZ dye removal first increases and then becomes almost constant as the contact time increases. This is due to the pores of NPs adsorbent getting filled up and starting to offer resistance to the diffusion of aggregated TZ dye molecules on the NPs
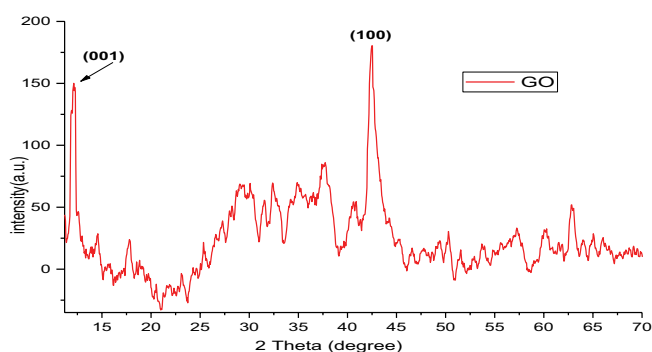

Fig. 3. X-ray diffraction pattern of graphene oxide nano-sheets.
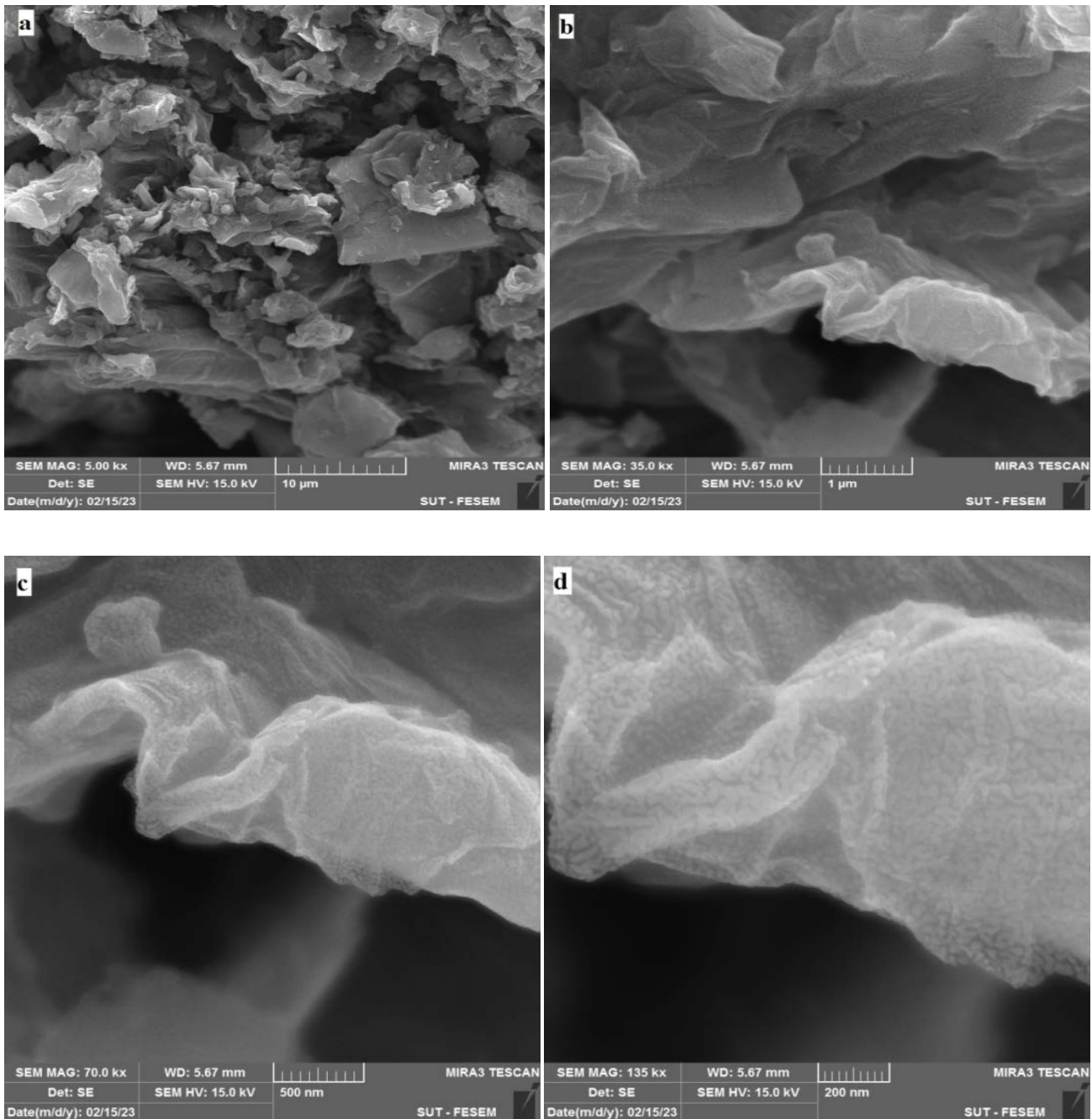

Fig. 4. X-ray diffraction patterns of AMCSD code (0007824) (a), Fe$_3$O$_4$ MNPs (b), GO/Fe$_3$O$_4$ MNPs (c), and GO (d).

Fig. 5. Field-emission scanning electron microscopy image at different magnifications (a) 10 μm, (b) 1 μm, (c) 500 nm and (d) 200 nm of GO nano-sheets.

adsorbent surface, which makes it almost impossible to diffuse TZ dye molecules deeper into the NPs adsorbent structure at higher energy sites [39]. Therefore, the addition of time no longer increases the removal of TZ dye (Fig. 13a).

3.2.2. Effect of adsorbent dose

Increasing the adsorbent dosage leads to an increase in the removal efficiency, due to the availability of an increased number of active adsorption sites. In this study, the percentage removal increased from 62.8 to 71.6 for Fe_3O_4 MNPs and from 64.8 to 81.4 for GO/Fe_3O_4 MNPs with increases in the adsorbent dose from 0.01 to 0.15 g for each adsorbent NPs when all other parameters were kept constant at 60 min, 25 mg/L, pH 7.3, and 298 K (Fig. 13b).

3.2.3. Effect of pH

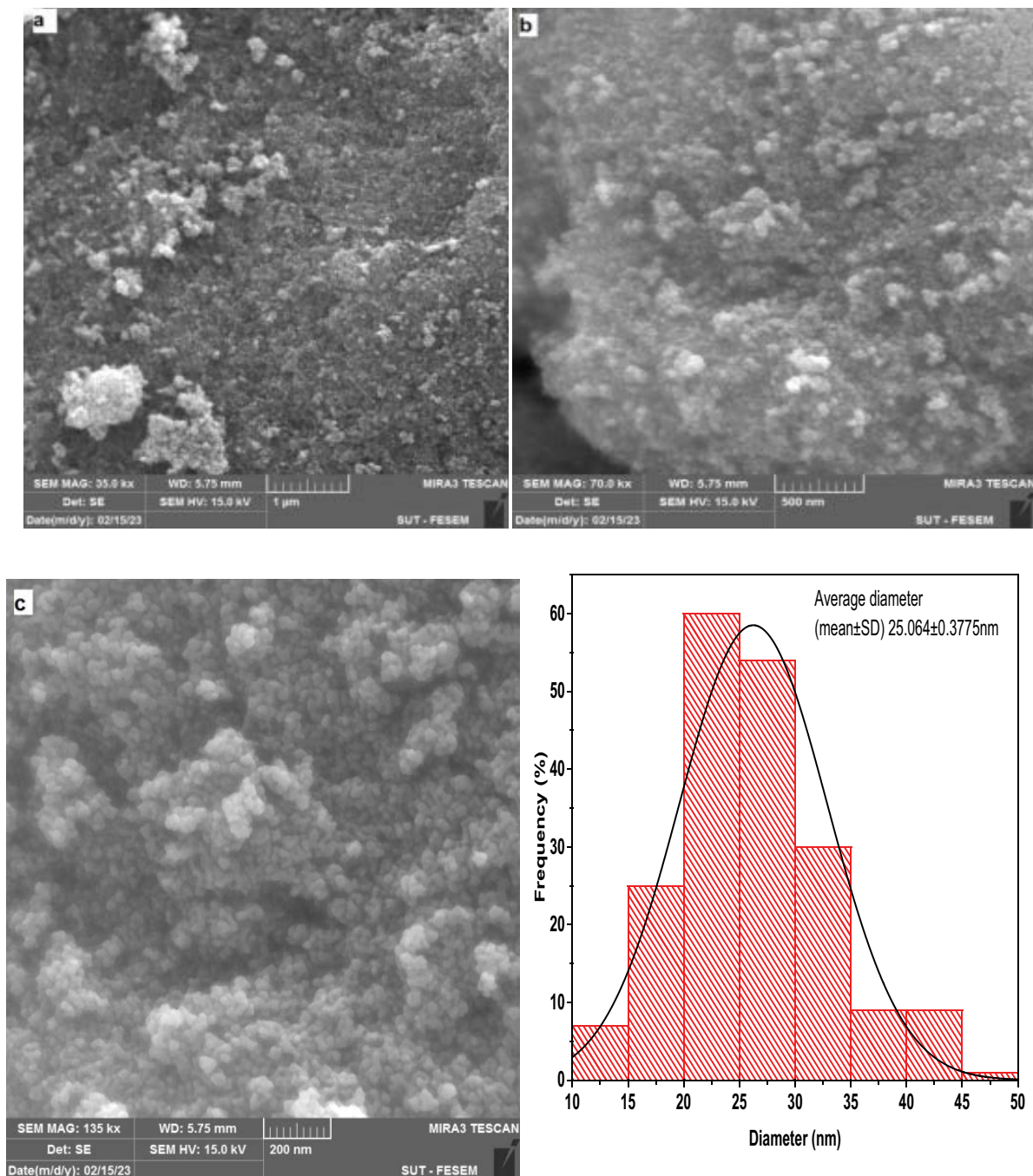The solution pH can affect the molecular structure of both the TZ dye and NPs adsorbent surface. The presence

Fig. 6. Field-emission scanning electron microscopy image at different magnifications (a) 1 μm, (b) 500 nm, (c) 200 nm and (d) particle-size distribution histogram of Fe_3O_4 NPs.

of different functional groups on the surface of both TZ dye and MNPs adsorbent may produce different charges at various pH ranges, leading to protonation/deprotonation and electrostatic interaction between the charged TZ dye and MNPs adsorbent [40]. The dissociation of TZ dye in aqueous solution can be represented by the chemical Eqs. (3)–(5):

$$Na_3TZ_{(s)} \rightarrow 3Na^+_{(aq)} + TZ^{3-}_{(aq)} \tag{3}$$

At the basic medium, there is competition between OH^- and TZ^{3-} toward the adsorption sites, so the removal percentage of TZ dye decreases onto MNPs.

$$MNPs\text{-}OH + OH^- \rightarrow MNPs\text{-}O^- + H_2O \tag{4}$$

At acidic medium, the MNPs surface was surrounded by H^+ ions led to increases in the attraction between the anionic surface of MNPs and TZ^{3-}, so the removal percentage of TZ dye increases onto MNPs.
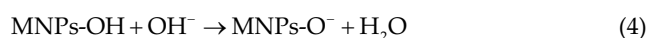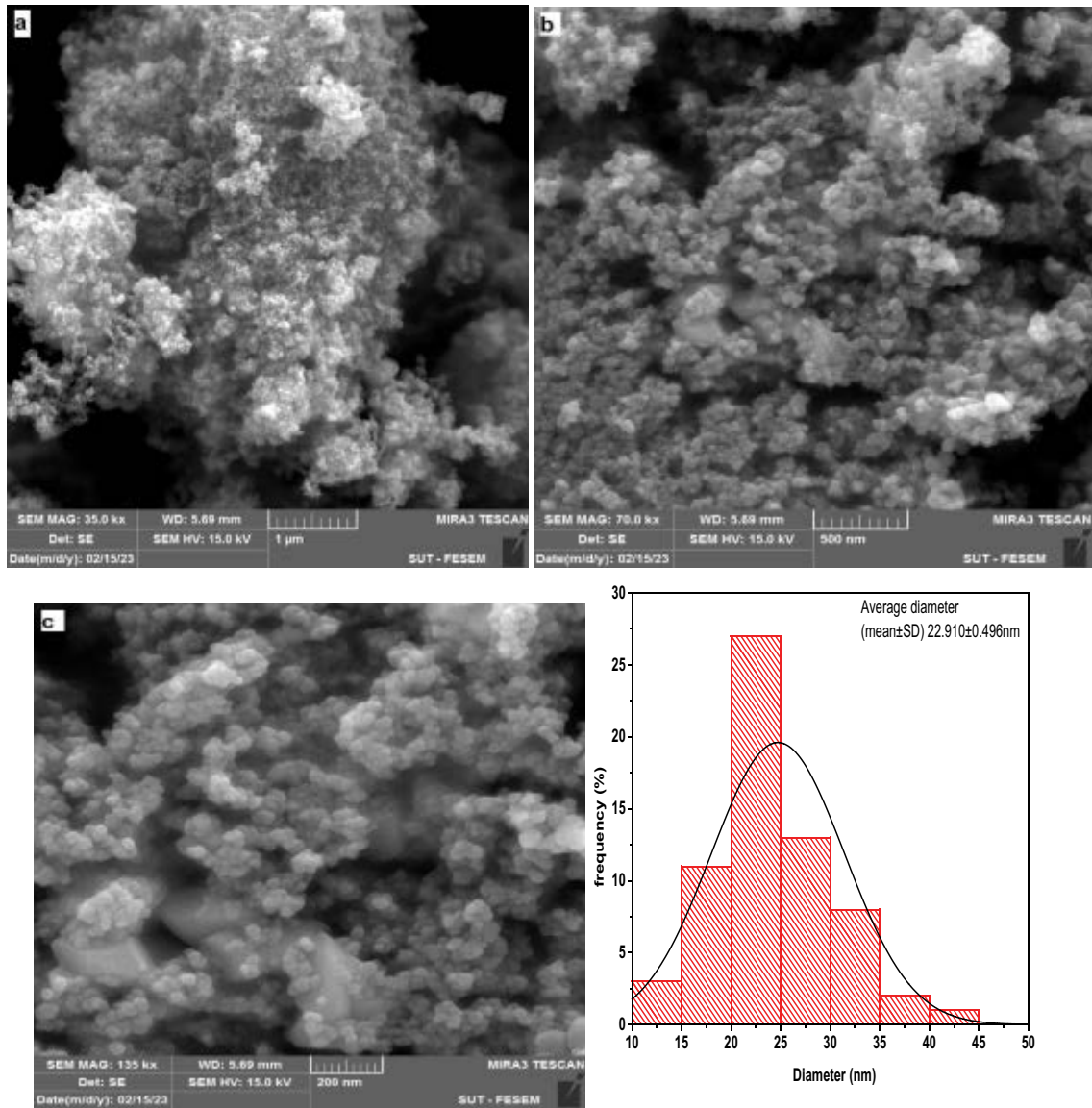
Fig. 7. Field-emission scanning electron microscopy image at different magnifications (a) 1 μm, (b) 500 nm, (c) 200 nm and (d) particle-size distribution histogram of GO/Fe$_3$O$_4$ NPs.

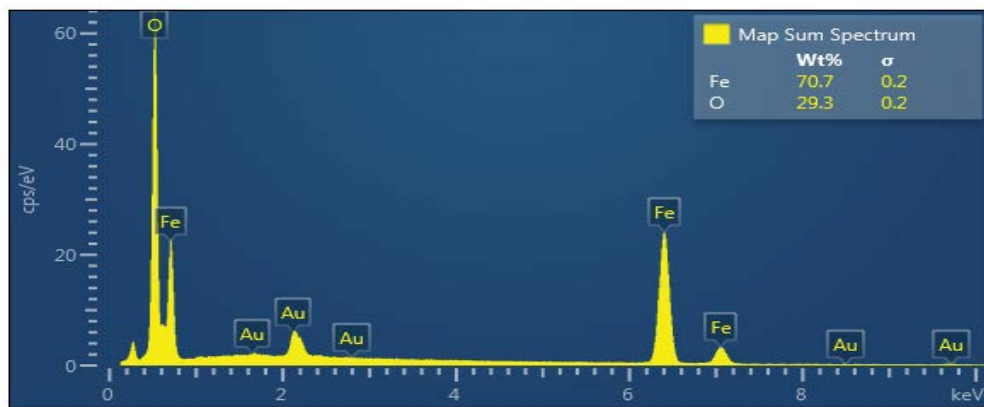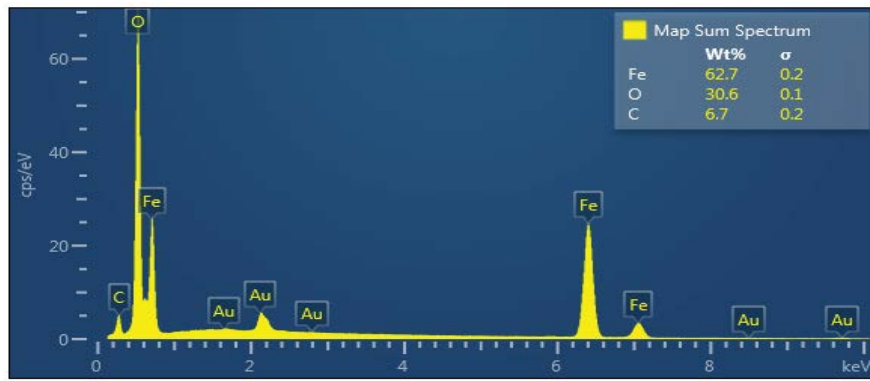Fig. 8. Energy-dispersive X-ray spectra of the Fe$_3$O$_4$ NPs.

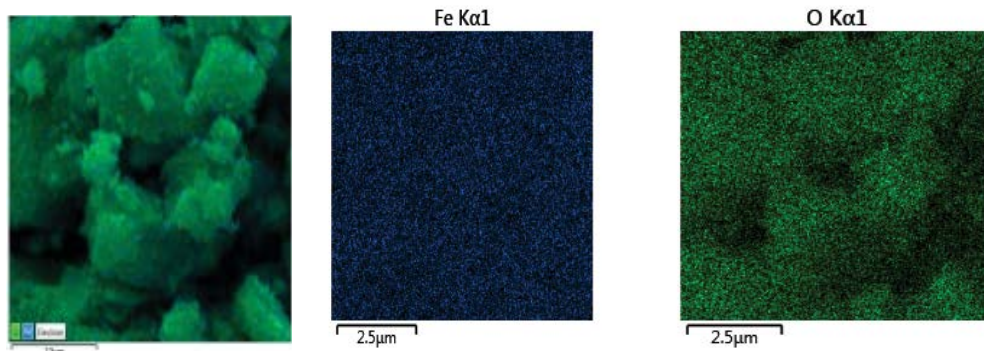Fig. 9. Energy-dispersive X-ray spectra of the GO/Fe$_3$O$_4$ MNPs.

Fig. 10. Energy-dispersive X-ray spectroscopy-map of elements in the structure of Fe$_3$O$_4$ NPs.
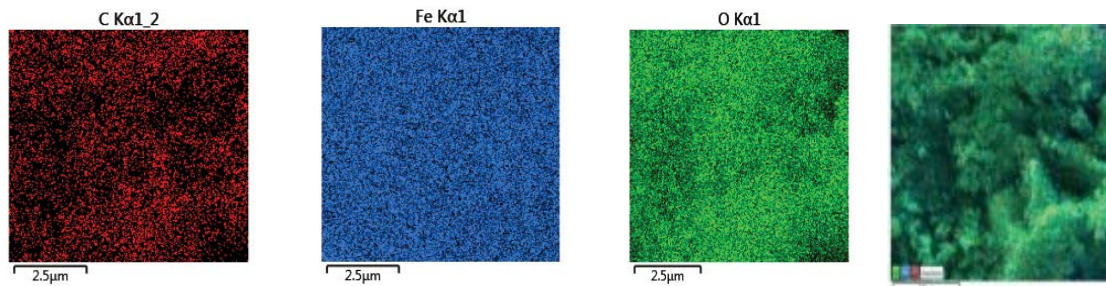

Fig. 11. Energy-dispersive X-ray spectroscopy-map of elements in the structure of GO/Fe$_3$O$_4$ MNPs.
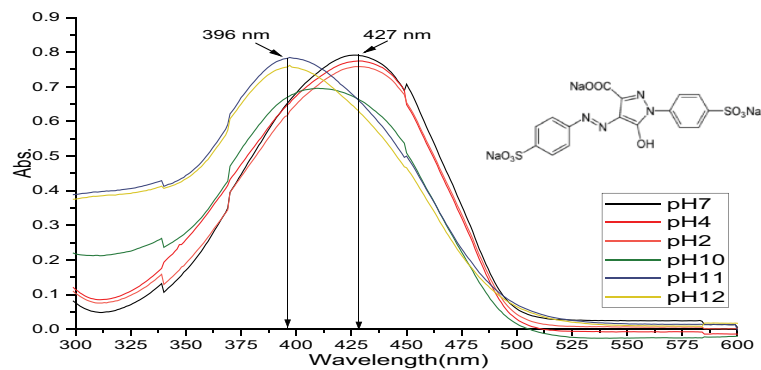

Fig. 12. Absorption spectra of tartrazine dye in the pH range from 2 to 12.
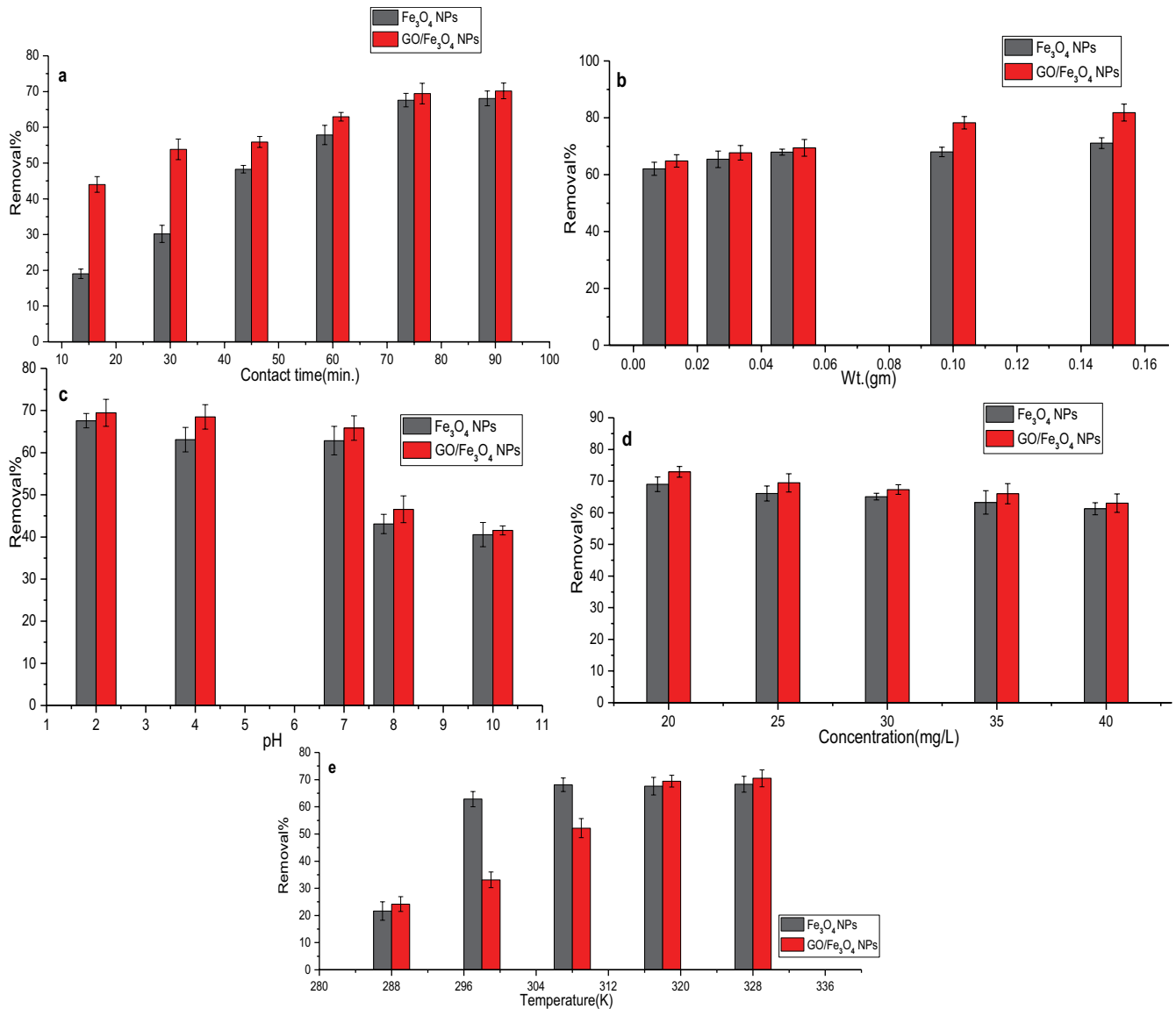
Fig. 13. Optimum conditions for tartrazine dye removal onto MNPs surfaces: (a) effect contact time, (b) effect weight of MNPs surfaces, (c) effect of pH, (d) effect of initial concentration and (e) effect of temperature.

$$\text{MNPs-OH} + \text{H}_3\text{O} \rightarrow \text{MNPs-OH}_2^+ + \text{H}_2\text{O} \tag{5}$$

Therefore, the adsorption mechanism of TZ dye onto the surface of MNPs is related to electrostatic attraction [13,41]. The experimental values showed that the adsorption process rises immaculately up to 78.5% for Fe_3O_4 MNPs and 80% for GO/Fe_3O_4 MNPs when the pH is 2 and other parameters were kept constant at (contact time 60 min, 0.01 g, 25 mg/L and 298 K) (Fig. 13c).

3.2.4. Effect of initial concentration

The initial concentration of the TZ dye solution is very important (Fig. 13d). Five different initial concentrations of TZ dye (20, 25, 30, 35 and 40 mg/L) were studied. Other parameters were kept constant at (contact time 60 min, 0.05 g, pH 7.3 and 298 K). The removal of dye is rapid in the

initial stages but it slows down gradually. This may be due to the availability of vacant surface sites during the preliminary stage of adsorption, and after a certain time period, the vacant sites get occupied by dye molecules which lead to creating a repulsive force between the TZ dye on the MNPs surface and in the bulk phase [42].

3.2.5. Effect of temperature

Five different temperatures (288, 298, 308, 318, and 328 K) were used to study the effect of temperature on the removal of TZ dye. Other parameters were kept constant at (contact time 60 min, 0.05 g, pH 7.3, and 25 mg/L). The percentage removal increased with increasing temperature from 21.6 to 76.0 and 24.2 to 79.2 for the adsorption of TZ dye onto Fe_3O_4 NPs and GO/Fe_3O_4 NPs, respectively. Furthermore, increasing heat leads to the interaction between TZ dye

and the surface of NPs being stronger than between the TZ dye and water molecules in the solution. Thus, the highest efficiency of adsorption was found at 318 K (Fig. 13e).

3.3. Adsorption isotherms

The ability of adsorbate molecules to distribute between the liquid and solid phases at the equilibrium state of the adsorption process is called the adsorption isotherm [43]. The Langmuir, Freundlich, and Dubinin–Radushkevich isotherms were used to describe the adsorption behavior of TZ dye onto Fe_3O_4 MNPs and GO/Fe_3O_4 MNPs (Table 2). The Langmuir isotherm explains the adsorption mechanism with a single adsorption layer and identifies the distribution of TZ dye between the solid and liquid phases. The Freundlich isotherm is an empirical equation that describes adsorption on surfaces with varying adsorption capacities, where adsorption occurs heterogeneously. The Dubinin–Radushkevich isotherm is based on the assumption of

adsorption taking place on a heterogeneous surface and provides information about the adsorption nature (physical or chemical) and the adsorption-free energy (E) [44]. The mean free energy (E) could be estimated by using the β parameter ($E = β$). E could distinguish the type of adsorption process. When $E < 8$ kJ/mol, it indicates physical adsorption, and when 8 kJ/mol $< E <$ 16 kJ/mol, it suggests the chemical mechanism [42]. R^2 can be used as an indicator of how well the experimental data points fit the theoretical model. When comparing the fitting quality of the Langmuir, Freundlich, and Dubinin–Radushkevich isotherms using R^2, a higher R^2 value generally suggests a better fit between the model and the experimental data (Tables 3 and 4). The isotherm with a higher R^2 value would indicate a better fit to the data (Fig. 14). It was noticed that TZ adsorption on Fe_3O_4 MNPs and GO/Fe_3O_4 MNPs is quite consistent with the Langmuir model at 313 K but not with the Freundlich or Dubinin–Radushkevich model. The separation factor (R_L) is a dimensionless parameter used to

Table 2
Linear expressions of isotherm models

Isotherm model	Equation	Linearized form	Plot	Parameters	References
Langmuir	$q_e = q_mK_LC_e/(1 + K_LC_e)$	$1/q_e = (1/K_Lq_mC_e) + (1/q_m)$	C_e/q_e vs. C_e	q_m = (intercept)$^{-1}$, K_L = intercept/slope	[48]
Freundlich	$q_e = K_F(C_e)^{1/n}$	$\log q_e = \log K_F + n^{-1}\log C_e$	$\log q_e$ vs. $\log C_e$	K_F = exp(intercept), $1/n$ = slope	[49]
Dubinin–Radushkevich	$q_e = q_{mexp}(-βε^2)$ $ε = RT\ln(1 + C_e^{-1})$	$\ln q_e = \ln q_m - βε^2$	$\ln q_e$ vs. $ε^2$	q_m = exp(intercept), β = −slope	[50]

q_e, q_m, q_t (mg/g) is the capacity at equilibrium, saturated, and at time t sorption; C_e (mg/L) is the concentration at equilibrium; n is heterogeneity of site energies; ε (J/mol) is the Polanyi potential; β (mol²/kJ²) is the Dubinin–Radushkevich constant; R (8.314 J/K·mol) is the gas constant; T (K) is the temperature.

Table 3
Isotherm constants for tartrazine dye adsorption at different temperatures onto Fe_3O_4 MNPs

Temperature (K)	Langmuir isotherm model			Freundlich isotherm model			Dubinin–Radushkevich isotherm model			
	q_L	K_L	R_L^2	K_F	n_F	R_F^2	q_{D-R}	$β_{D-R}$	E_{D-R}	R_{D-R}^2
288	0.105	63.026	0.612	0.193	0.607	0.893	9.365	7×10^{-5}	84.515	0.795
298	0.195	63.123	0.977	0.289	0.648	0.992	14.310	6×10^{-5}	691.287	0.935
308	1.154	13.323	0.985	1.563	2.538	0.984	10.946	1×10^{-5}	223.606	0.886
318	1.540	9.544	0.998	1.736	2.967	0.995	11.427	8×10^{-6}	250	0.952
328	0.120	99.939	0.899	2.229	6.535	0.873	10.686	3×10^{-6}	408.249	0.770

Table 4
Isotherm constants for tartrazine dye adsorption at different temperatures onto GO/Fe_3O_4 MNPs

| Temperature (K)	Langmuir isotherm model			Freundlich isotherm model			Dubinin–Radushkevich isotherm model			
	q_L	K_L	R_L^2	K_F	n_F	R_F^2	q_{D-R}	$β_{D-R}$	E_{D-R}	R_{D-R}^2
288	0.497	0.037	0.730	15.302	6.896	0.832	7.721	2×10^{-5}	158.114	0.701
298	0.588	20.226	0.829	25.584	7.751	0.841	7.667	2×10^{-5}	158.114	0.714
308	14.705	1.152	0.998	2.935	10.638	0.882	16.006	9×10^{-7}	745.360	0.944
318	333.333	0.6	0.999	3.164	3.558	0.975	26.575	4×10^{-7}	1118	0.831
328	45.454	0.431	0.983	3.377	20.833	0.777	18.896	1×10^{-7}	2236.067	0.820
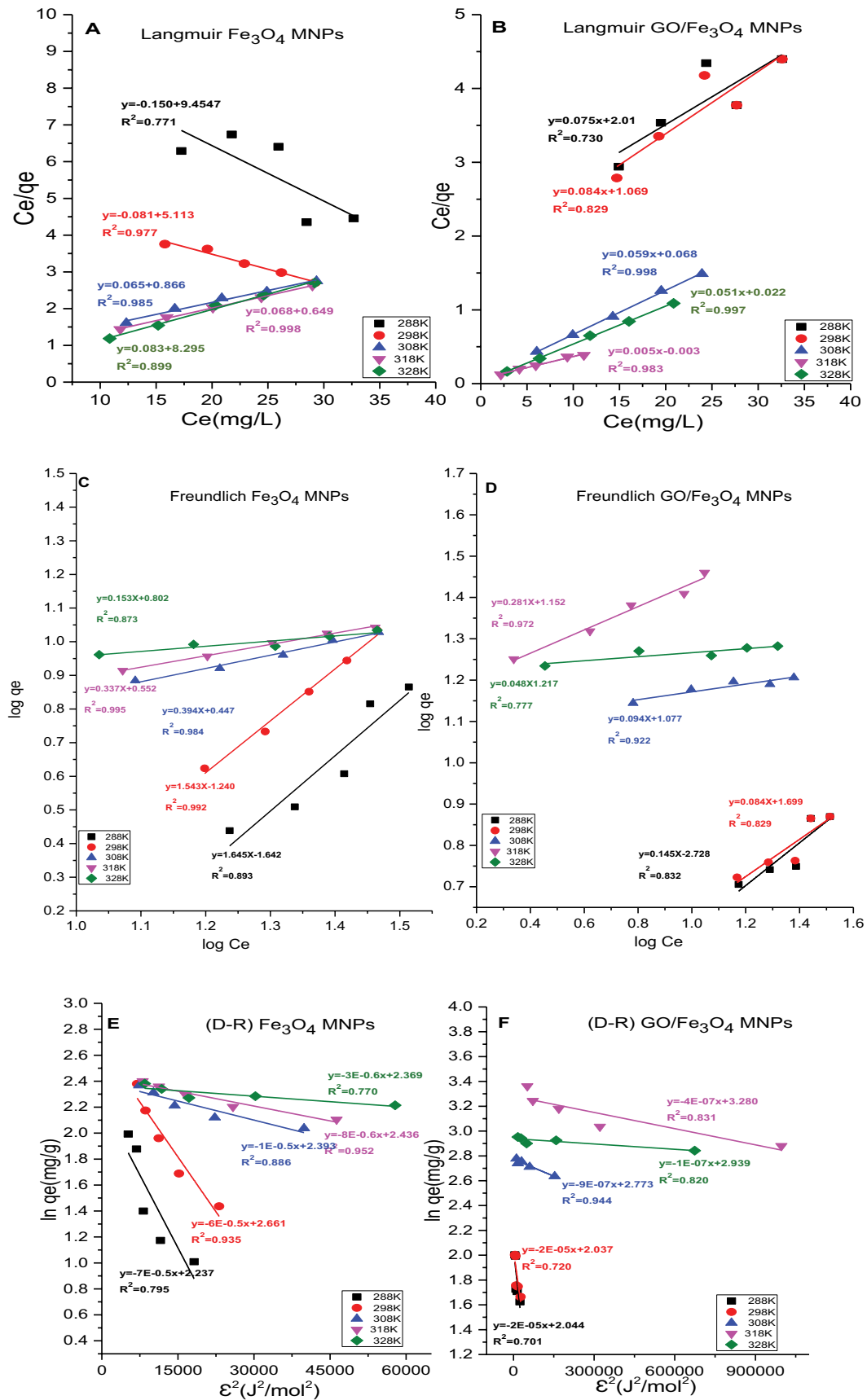
Fig. 14. Isotherm models of Langmuir I (a,b), Freundlich (c,d), and Dubinin–Radushkevich (e,f) at 313 K.

evaluate the favorability of adsorption according to the Langmuir isotherm. The R_L value can be interpreted [46,47]:

$R_L = 1$: indicates linear adsorption;
$R_L > 1$: indicates unfavorable adsorption;
$R_L = 0$: indicates irreversible adsorption;
$0 < R_L < 1$: indicates favorable adsorption.

Moreover, R_L could be calculated:

$$R_L = \frac{1}{\left(1 + K_L C_0\right)} \tag{6}$$

where R_L is the separation factor, K_L is the Langmuir constant, and C_0 (mg/L) is the initial concentration of the TZ dye. In this study, all the values of R_L were lies between 0 and 1 which confirmed that the adsorption of TZ dye onto Fe_3O_4 MNPs and GO/Fe_3O_4 MNPs was favorable at different temperatures (Table 5).

3.4. Adsorption thermodynamics

The study of the thermodynamic properties of adsorption processes is done by adsorption thermodynamics parameters. Adsorption thermodynamics is an important tool for understanding and designing adsorption systems [51].

The van't Hoff equation is a useful tool for calculating the thermodynamic parameters of adsorption. It could be calculated from next equations:

$$\ln K_{eq} = \frac{\Delta S}{R} + \frac{\Delta H}{RT} \tag{7}$$

$$K_{eq} = \frac{q_e}{C_e} \tag{8}$$

The van't Hoff equation can be used to calculate the thermodynamic parameters of adsorption by plotting $\ln K_{eq}$ vs. $1/T$. The slope of the plot is equal to $-\Delta H°/R$ and the intercept is equal to $\Delta S°/R$ (Fig. 15). Once the $\Delta H°$ and $\Delta S°$ values are known, the $\Delta G°$ can be calculated using Eq. (9):

$$\Delta G° = \Delta H° - T\Delta S° \tag{9}$$

where T: is the absolute temperature (K), K_{eq}: is the ability of adsorbate to retain and a measure of its movement within the solution, R: is the general of gases constant (8.314 J/mol K), q_e (mg/g) is the equilibrium capacity of adsorption.

Table 5
Dimensionless separation factor R_L at different temperatures

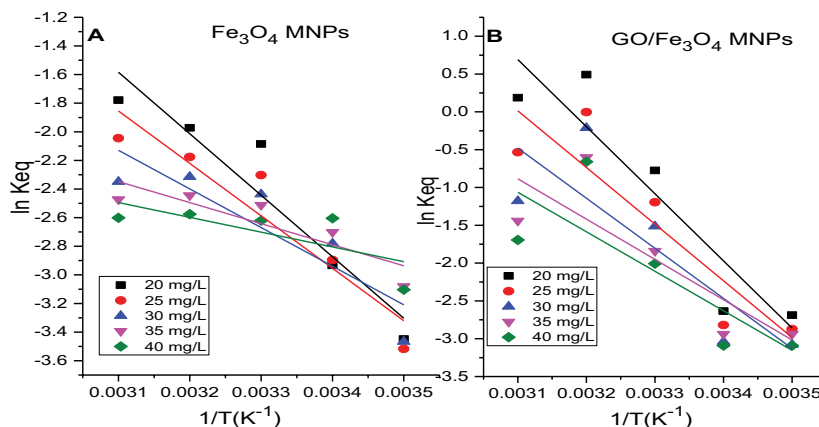|	Tartrazine (mg/L)	Temperature (K)				
		288 K	298 K	308 K	318 K	328 K
Fe_3O_4 NPs	288	0.00079	0.00079	0.00373	0.00521	0.00050
	298	0.00063	0.00063	0.00299	0.00417	0.00040
	308	0.00052	0.00052	0.00249	0.00348	0.00033
	318	0.00045	0.00045	0.00213	0.00298	0.00028
	328	0.00039	0.00039	0.00187	0.00261	0.00025
GO/Fe_3O_4 NPs	288	0.57280	0.00246	0.04158	0.07692	0.10388
	298	0.51753	0.00197	0.03354	0.06250	0.084872
	308	0.47198	0.00164	0.028110	0.05263	0.07174
	318	0.43381	0.00141	0.024191	0.04545	0.06212
	328	0.401341	0.00123	0.021231	0.04000	0.05478

Fig. 15. Van't Hoff plots for the adsorption tartrazine dye onto (a) Fe_3O_4 MNPs and (b) GO/Fe_3O_4 MNPs at different temperature.

The positive values of the Gibbs free energy $\Delta G°$ confirm that the adsorption of TZ dye onto MNPs is non-spontaneous, meaning that it does not occur without the input of energy. The positive values of $\Delta H°$ confirm the endothermic nature of the adsorption process for both MNPs, meaning that heat is absorbed during the adsorption process [52]. The positive values of the entropy change $\Delta S°$ suggest an increase in randomness at the solid/solution interface during the adsorption process (Table 6).

3.5. Adsorption kinetics

In order to characterize the mechanism of adsorption and the potential rate, four models like pseudo-first-order, pseudo-second-order, may be used to test the experimental data. At pH 2, adsorbent dosage of 0.05 g/10 mL, and starting TZ dye concentrations of 25 mg/L, kinetic analysis for the two models was carried out at 318 K. The equation for pseudo-first-order is expressed as [53].

$$\ln\left(q_e - q_t\right) = \ln q_e - K_1 t \tag{10}$$

where q_t is the amount of TZ dye adsorbed at time t (min), q_e is the amount of TZ dye adsorbed at equilibrium (mg/g),

and K_1 is the pseudo-first-order rate constant for the adsorption process (min^{-1}). The plot of $\ln(q_e - q_t)$ vs. t gives a straight line. So, K_1 can be calculated as 1/slope and q_e can be determined as exp$^{(intercept)}$.

The equation for pseudo-second-order is given by [54,55]:

$$\frac{t}{q_t} = \frac{1}{K_2 q_e^2} + \left(\frac{1}{q_e}\right)t \tag{11}$$

where q_t (mg/g) is the amount of the TZ dye adsorbed at any time, q_e (mg/g) is the amount of the dye adsorbed at equilibrium, t is the adsorption time (min), K_2 is the rate constant of the pseudo-second-order (g/mg·min).

The plot of t/q_t vs. t gives a straight line. Therefore, K_2 is calculated as (slope^2)/intercept and q_e can be determined as 1/slope (Fig. 16).

In Table 7, the values of the correlation coefficient R^2 for pseudo-first-order are 0.966 and 0.955, which are lower than the R^2 values for the pseudo-second-order kinetic model (0.970 and 0.998). From these values, it can be inferred that the adsorption of TZ dye on Fe_3O_4 MNPs and GO/Fe_3O_4 MNPs is nearly inapplicable with a pseudo-second-order kinetic model, whereas the adsorption of TZ dye onto both

Table 6
Thermodynamic parameters for the adsorption of tartrazine dye onto MNPs

| Adsorbent	C_o	Slope	Intercept	$\Delta H°$ (kJ/mol)	$\Delta S°$ (J/mol)	$\Delta G°$ (kJ/mol)				
						288 K	298 K	308 K	318 K	328 K
Fe_3O_4 MNPs	20	−4,299.035	11.743	35,742.178	97.634	7,623.573	6,647.233	5,670.892	4,694.552	3,718.212
	25	−3,664.848	9.50665	30,469.553	79.038	7,706.526	6,916.143	6,125.760	5,335.378	4,544.995
	30	−2,700.704	6.24307	22,453.655	51.904	7,505.049	6,986.000	6,466.951	5,947.902	5,428.853
	35	−1,472.279	2.21653	12,240.535	18.428	6,933.205	6,748.922	6,564.640	6,380.358	6,196.075
	40	−1,032.890	0.7073	8,587.454	5.880	6,893.873	6,835.068	6,776.263	6,717.458	6,658.653
GO/Fe_3O_4 MNPs	20	−8,874.928	28.20376	73,786.154	234.486	6,254.169	3,909.308	1,564.447	−780.412	−3,125.273
	25	−7,491.866	23.23829	62,287.374	193.203	6,644.868	4,712.837	2,780.805	848.774	−1,083.256
	30	−6,624.403	20.05614	55,075.289	166.746	7,052.226	5,384.758	3,717.291	2,049.823	382.356
	35	−5,329.049	15.634	44,305.717	129.984	6,870.089	5,570.241	4,270.393	2,970.545	1,670.697
	40	−5,224.258	15.131	43,434.482	125.805	7,202.488	5,944.432	4,686.377	3,428.322	2,170.266
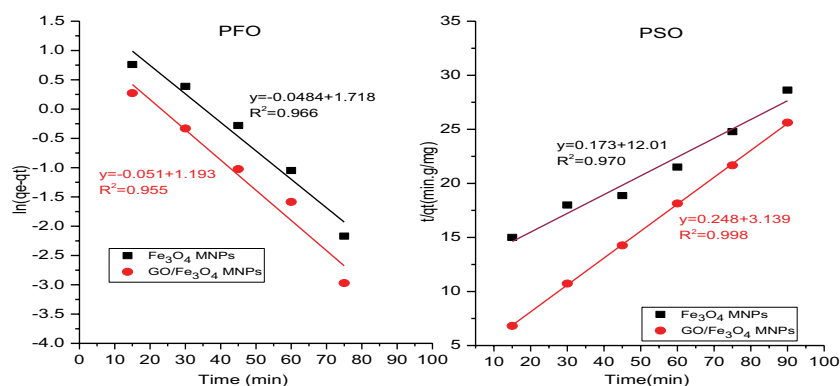
Fig. 16. Pseudo-first-order kinetic model and pseudo-second-order kinetic model linear form for the adsorption of (25 mg/L) tartrazine dye on Fe_3O_4 MNPs and GO/Fe_3O_4 MNPs at 318 K.

Table 7
Kinetic model parameters for (25 mg/L) tartrazine dye on Fe_3O_4 MNPs and GO/Fe_3O_4 MNPs at 318 K

Adsorbent	Pseudo-first-order					Pseudo-second-order				
	Slope	Intercept	K_1	q_e	R^2	Slope	Intercept	K_2	q_e	R^2
Fe_3O_4 MNPs	−0.048	1.714	0.048	5.573	0.966	0.173	12.01	0.0025	5.780	0.970
GO/Fe_3O_4 MNPs	−0.051	1.193	0.051	3.296	0.955	0.248	3.139	0.0195	4.032	0.998

Table 8
Represents the comparison of the optimum adsorption conditions of different adsorbents for tartrazine dye

| Adsorbents	Time (min.)	pH	Temperature	Isotherm	Pollutant	References
Montmorillonite K10 modified by hexadecylamine surfactant (Mt-HDA)	30	4	318 K	Langmuir	Aqueous phase	[13]
Surfactant-ionic liquid bi-functionalization of chitosan beads CS-CTAB-AL	45	10	318 K	Langmuir	Polluted water	[57]
Biochar-mediated zirconium ferrite nano composites	360	2	303 K	–	Textile wastewater	[58]
Copper coordinated dithiooxamide metal-organic framework (Cu-DTO MOF)	40	2	323 K	Freundlich	Aqueous solutions	[59]
Sawdust	70	3	–	Langmuir	Aqueous solution	[60]
Carbon nanotubes decorated with silver nanoparticles Ag/CNTs	60	3	–	Langmuir	Aqueous solution	[61]
Activated carbon derived from cassava sievate biomass	90	1	313 K	–	Wastewaters	[62]
Fe_3O_4 MNPs and GO/Fe_3O_4 MNPs	60	2	318 K	Langmuir	Aqueous solution	This study

MNPs is applicable with the pseudo-second-order kinetic model. The order of arrangement for the applicability of these kinetic models is as follows: pseudo-second-order model > pseudo-first-order.

3.6. Reusability of MNPs

The key factor for evaluating the stability and efficiency of the adsorbent and desorption process is reusability. The Fe_3O_4 MNPs and GO/Fe_3O_4 MNPs sorbent were found to be reusable after a washing step with distilled water five times and a drying step at room temperature. The results obtained in the subsequent experiments indicate that the MNPs can be reused at least 5 times without a significant loss of extraction efficiency (Fig. 17). Fe_3O_4 MNPs and GO/Fe_3O_4 MNPs are considered green chemistry adsorbents because they can be recovered and reused using an external magnet. They do not require the use of filter papers, centrifugation steps, or purification steps, which reduce time and energy consumption, making the adsorption method simpler and low-cost, achieving ease of process [56].

3.7. Comparison with other adsorbents

The adsorption conditions of previous studies such as contact time, pH, temperature, isotherm, and pollutant are listed in Table 8. It can observe that the adsorbent type played a significant role in effected onto the adsorption conditions.
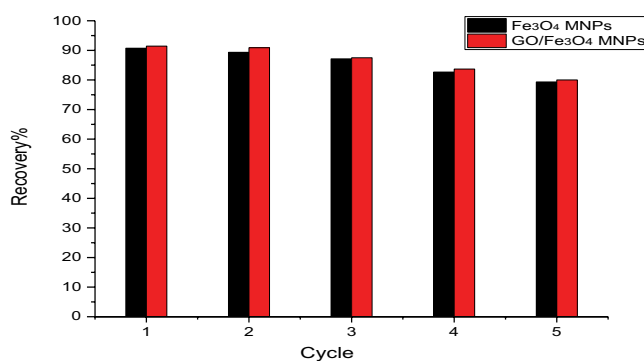
Fig. 17. Number of re-used of Fe_3O_4 MNPs and GO/Fe_3O_4 MNPs.

4. Conclusions

The photo-irradiation method was successfully used to synthesize Fe_3O_4 MNPs and GO/Fe_3O_4 MNPs in this study. These MNPs surfaces are highly effective absorbents for removing TZ dyes from aqueous solutions. The study investigated optimal conditions including contact time, surface amount, pH, dye concentration, and temperature. The adsorption isotherms of TZ onto Fe_3O_4 MNPs and GO/Fe_3O_4 MNPs were well-matched with the Langmuir model at 313 K. Furthermore, the separation factor (R_L) values indicated favorable adsorption of TZ on both MNPs surfaces at different temperatures. Thermodynamic studies revealed that the adsorption processes of TZ dye are endothermic,

non-spontaneous, and involve an increase in order at the interface for both MNPs surfaces. The pseudo-second-order rate kinetics suggests that both MNPs show promise as materials for removing TZ dye from aqueous solutions. Overall, the results confirm that Fe_3O_4 MNPs and GO/Fe_3O_4 MNPs are efficient, low-cost, and stable adsorbents.

Conflict of interest

The authors declare that there are no conflicts of interest regarding the publication of this manuscript.

References

[1] L. Mabuza, N. Sonnenberg, N. Marx-Pienaar, Natural versus synthetic dyes: consumers' understanding of apparel coloration and their willingness to adopt sustainable alternatives, Resour. Conserv. Recycl. Adv., 18 (2023) 200146, doi: 10.1016/j.rcradv.2023.200146.

[2] H.B. Slama, A.C. Bouket, Z. Pourhassan, F.N. Alenezi, A. Silini, H. Cherif-Silini, T. Oszako, L. Luptakova, P. Golińska, L. Belbahri, Diversity of synthetic dyes from textile industries, discharge impacts and treatment methods, Appl. Sci., 11 (2021) 6255, doi: 10.3390/app11146255.

[3] M.A. Ahmed, A.S. Al-Khalifa, D.M. Al-Nouri, M.F.S. El-Din, Dietary intake of artificial food color additives containing food products by school-going children, Saudi J. Biol. Sci., 28 (2021) 27–34.

[4] S. Sahnoun, M. Boutahala, Adsorption removal of tartrazine by chitosan/polyaniline composite: kinetics and equilibrium studies, Int. J. Biol. Macromol., 114 (2018) 1345–1353.

[5] L. Aoudjit, P.M. Martins, F. Madjene, D.Y. Petrovykh, S. Lanceros-Mendez, Photocatalytic reusable membranes for the effective degradation of tartrazine with a solar photoreactor, J. Hazard. Mater., 344 (2018) 408–416.

[6] K.B. Errahmani, O. Benhabiles, S. Bellebia, Z. Bengharez, M. Goosen, H. Mahmoudi, Photocatalytic nanocomposite polymer-TiO_2 membranes for pollutant removal from wastewater, Catalysts, 11 (2021) 402, doi: 10.3390/catal11030402.

[7] G. Donoso, J.R. Dominguez, T. González, S. Correia, E.M. Cuerda-Correa, Electrochemical and sonochemical advanced oxidation processes applied to tartrazine removal. Influence of operational conditions and aqueous matrix, Environ. Res., 202 (2021) 111517, doi: 10.1016/j.envres.2021.111517.

[8] A.V. Russo, B.G. Merlo, S.E. Jacobo, Adsorption and catalytic degradation of Tartrazine in aqueous medium by a Fe-modified zeolite, Cleaner Eng. Technol., 4 (2021) 100211, doi: 10.1016/j.clet.2021.100211.

[9] R. Scott, P. Mudimbi, M.E. Miller, M. Magnuson, S. Willison, R. Phillips, W.F. Harper Jr., Advanced oxidation of tartrazine and brilliant blue with pulsed ultraviolet light emitting diodes, Water Environ. Res., 89 (2017) 24–31.

[10] M. Assassi, F. Madjene, S. Harchouche, H. Boulfiza, Modeling and optimization of the photocatalytic degradation of Tartrazine in aqueous solution, Acta Period. Technol., 52 (2021) 133–145.

[11] S.K. Al-Dawery, Photo-catalyst degradation of tartrazine compound in wastewater using TiO_2 and UV light, J. Eng. Sci. Technol., 8 (2013) 683–691.

[12] F. Parolin, U.M. Nascimento, E.B. Azevedo, Microwave-enhanced UV/H_2O_2 degradation of an azo dye (tartrazine): optimization, colour removal, mineralization and ecotoxicity, Environ. Technol., 34 (2013) 1247–1253.

[13] S.H. Tabrizi, B. Tanhaei, A. Ayati, S. Ranjbari, Substantial improvement in the adsorption behavior of montmorillonite toward Tartrazine through hexadecylamine impregnation, Environ. Res., 204 (2022) 111965, doi: 10.1016/j.envres.2021.111965.

[14] H.I. Albroomi, M.A. Elsayed, A. Baraka, M.A. Abdelmaged, Batch and fixed-bed adsorption of tartrazine azo-dye onto activated carbon prepared from apricot stones, Appl. Water Sci., 7 (2017) 2063–2074.

[15] E.H. Khader, T.J. Mohammed, T.M. Albayati, Comparative performance between rice husk and granular activated carbon for the removal of azo tartrazine dye from aqueous solution, Desal. Water Treat., 229 (2021) 372–383.

[16] S. Perveen, R. Nadeem, F. Nosheen, L. Tongxiang, T. Anwar, Synthesis of biochar-supported zinc oxide and graphene oxide/zinc oxide nanocomposites to remediate tartrazine dye from aqueous solution using fixed-bed column reactor, Appl. Nanosci., 12 (2022) 1491–1505.

[17] S. Perveen, R. Nadeem, F. Nosheen, M.I. Asjad, J. Awrejcewicz, T. Anwar, Biochar-mediated zirconium ferrite nanocomposites for tartrazine dye removal from textile wastewater, Nanomaterials, 12 (2022) 2828, doi: 10.3390/nano12162828.

[18] M. Ur Rehman, A. Manan, M. Uzair, A.S. Khan, A. Ullah, A.S. Ahmad, A.H. Wazir, I. Qazi, M.A. Khan, Physicochemical characterization of Pakistani clay for adsorption of methylene blue: kinetic, isotherm and thermodynamic study, Mater. Chem. Phys., 269 (2021) 124722, doi: 10.1016/j.matchemphys.2021.124722.

[19] A. Haleem, M. Javaid, R.P. Singh, S. Rab, R. Suman, Applications of nanotechnology in medical field, Global Health J., 7 (2023) 70–77.

[20] R.F. Abbas, M.J.M. Hassan, A.M. Rheima, Magnetic solid phase extraction for determination of dyes in food and water samples, Indones. J. Chem., 4 (2023) 1181–1198.

[21] A. Hajighasemkhan, L. Taghavi, E. Moniri, A.H. Hassani, H.A. Panahi, Adsorption kinetics and isotherms study of 2,4-dichlorophenoxyacetic acid by 3dimensional/graphene oxide/magnetic from aquatic solutions, Int. J. Environ. Anal. Chem., 102 (2022) 1171–1191.

[22] M. Shafaati, M. Miralinaghi, R.H.S.M. Shirazi, E. Moniri, The use of chitosan/Fe_3O_4 grafted graphene oxide for effective adsorption of rifampicin from water samples, Res. Chem. Intermed., 46 (2020) 5231–5254.

[23] A.F. Kamil, H.I. Abdullah, A.M. Rheima, W.M. Khamis, Modification of hummers presses for synthesis graphene oxide nano-sheets and graphene oxide/Ag nanocomposites, J. Ovonic Res., 17 (2021) 253–259.

[24] A.F. Kamil, H.I. Abdullah, A.M. Rheima, Fabrication of dye-sensitized solar cells and synthesis of $CuNiO_2$ nanostructures using a photo-irradiation technique, J. Nanostruct., 12 (2022) 144–159.

[25] T. Taher, A. Munandar, N. Mawaddah, M. Syamsuddin Wisnubroto, P.M.S.B.N. Siregar, N.R. Palapa, A. Lesbani, Y.G. Wibowo, Synthesis and characterization of montmorillonite – mixed metal oxide composite and its adsorption performance for anionic and cationic dyes removal, Inorg. Chem. Commun., 147 (2023) 110231, doi: 10.1016/j.inoche.2022.110231.

[26] R.F. Abbas, H.K. Hami, N.I. Mahdi, A.A. Waheb, Removal of Eriochrome Black T dye by using Al_2O_3 nanoparticles: central composite design, isotherm and error analysis, Iran. J. Sci. Technol., Trans. A: Sci., 44 (2020) 993–1000.

[27] P.T. Lan Huong, N.T. Huyen, C.D. Giang, N. Tu, V.N. Phan, N.V. Quy, T.Q. Huy, D.T.M. Hue, H.D. Chinh, A.-T. Le, Facile synthesis and excellent adsorption property of $GO-Fe_3O_4$ magnetic nanohybrids for removal of organic dyes, J. Nanosci. Nanotechnol., 16 (2016) 9544–9556.

[28] M.S. Raghu, K. Yogesh Kumar, M.K. Prashanth, B.P. Prasanna, R. Vinuth, C.B. Pradeep Kumar, Adsorption and antimicrobial studies of chemically bonded magnetic graphene oxide-Fe_3O_4 nanocomposite for water purification, J. Water Process Eng., 17 (2017) 22–31.

[29] A.-S. Al-Sherbini, M. Bakr, I. Ghoneim, M. Saad, Exfoliation of graphene sheets via high energy wet milling of graphite in 2-ethylhexanol and kerosene, J. Adv. Res., 8 (2017) 209–215.

[30] H. Jeddi, R. Rasuli, M.M. Ahadian, B. Mehrabi, Carbon black-intercalated reduced graphene oxide electrode with graphene oxide separator for high-performance supercapacitor, J. Nanostruct., 9 (2019) 639–649.

[31] L. Yu, J. Chen, Z. Liang, W. Xu, L. Chen, D. Ye, Degradation of phenol using Fe_3O_4-GO nanocomposite as a heterogeneous photo-Fenton catalyst, Sep. Purif. Technol., 171 (2016) 80–87.

[32] M. Jannatin, G. Supriyanto, Abdulloh, W.A.W. Ibrahim, N.K. Rukman, Graphene oxide from bagasse/magnetite composite: preparation and characterization, IOP Conf. Ser.: Earth Environ. Sci., 217 (2019) 012007, doi: 10.1088/1755-1315/217/1/012007.

[33] J.J. Schuster, S. Will, A. Leipertz, A. Braeuer, Deconvolution of Raman spectra for the quantification of ternary high-pressure phase equilibria composed of carbon dioxide, water and organic solvent, J. Raman Spectrosc., 45 (2014) 246–252.

[34] K. Movlaee, M.R. Ganjali, P. Norouzi, G. Neri, Iron-based nanomaterials/graphene composites for advanced electrochemical sensors, Nanomaterials (Basel), 7 (2017) 406, doi: 10.3390/nano7120406.

[35] Y. Wei, B. Han, X. Hu, Y. Lin, X. Wang, X. Deng, Synthesis of Fe_3O_4 nanoparticles and their magnetic properties, Procedia Eng., 27 (2012) 632–637.

[36] A. Mayeen, L.K. Shaji, A.K. Nair, N. Kalarikkal, Chapter 12 – Morphological Characterization of Nanomaterials, S.M. Bhagyaraj, O.S. Oluwafemi, N. Kalarikkal, S. Thomas, Eds., Characterization of Nanomaterials: Advances and Key Technologies, Micro and Nano Technologies, Woodhead Publishing, 2018, pp. 335–364.

[37] A. Raza, U. Qumar, J. Hassan, M. Ikram, A. Ul-Hamid, J. Haider, M. Imran, S. Ali, A comparative study of dirac 2D materials, TMDCs and 2D insulators with regard to their structures and photocatalytic/sonophotocatalytic behavior, Appl. Nanosci., 10 (2020) 3875–3899.

[38] A.A. Issa, Y.S. Al-Degs, K. Mashal, R.Z. Al Bakain, Fast activation of natural biomasses by microwave heating, J. Ind. Eng. Chem., 21 (2015) 230–238.

[39] P. Sharma, H. Kaur, Sugarcane bagasse for the removal of Erythrosin B and methylene blue from aqueous waste, Appl. Water Sci., 1 (2011) 135–145.

[40] B. Priyadarshini, T. Patra, T.R. Sahoo, An efficient and comparative adsorption of Congo red and Trypan blue dyes on MgO nanoparticles: kinetics, thermodynamics and isotherm studies, J. Magnesium Alloys, 9 (2021) 478–488.

[41] H. Ouassif, E.M. Moujahid, R. Lahkale, R. Sadik, F.Z. Bouragba, E.M. Sabbar, M. Diouri, Zinc-aluminum layered double hydroxide: high efficient removal by adsorption of tartrazine dye from aqueous solution, Surf. Interfaces, 18 (2020) 100401, doi: 10.1016/j.surfin.2019.100401.

[42] S. Banerjee, M.C. Chattopadhyaya, Adsorption characteristics for the removal of a toxic dye, tartrazine from aqueous solutions by a low-cost agricultural by-product, Arabian J. Chem., 10 (2017) S1629–S1638.

[43] N.F. Al-Harby, E.F. Albahly, N.A. Mohamed, Kinetics, isotherm and thermodynamic studies for efficient adsorption of Congo red dye from aqueous solution onto novel cyanoguanidine-modified chitosan adsorbent, Polymers, 13 (2021) 4446, doi: 10.3390/polym13244446.

[44] M. Ghobadi, M. Gharabaghi, H. Abdollahi, Z. Boroumand, M. Moradian, $MnFe_2O_4$-graphene oxide magnetic nanoparticles as a high-performance adsorbent for rare earth elements: synthesis, isotherms, kinetics, thermodynamics and desorption, J. Hazard. Mater., 351 (2018) 308–316.

[45] Q. Hu, Z. Zhang, Application of Dubinin–Radushkevich isotherm model at the solid/solution interface: a theoretical analysis, J. Mol. Liq., 277 (2019) 646–648.

[46] Y. Miyah, A. Lahrichi, M. Idrissi, S. Boujraf, H. Taouda, F. Zerrouq, Assessment of adsorption kinetics for removal potential of Crystal Violet dye from aqueous solutions using Moroccan pyrophyllite, J. Assoc. Arab Univ. Basic Appl. Sci., 23 (2017) 20–28.

[47] G.Y. Abate, A.N. Alene, A.T. Habte, D.M. Getahun, Adsorptive removal of malachite green dye from aqueous solution onto activated carbon of *Catha edulis* stem as a low-cost bio-adsorbent, Environ. Res., 9 (2020) 1–13, doi: 10.1186/s40068-020-00191-4.

[48] A. Demir Delil, O. Gülçiçek, N. Gören, Optimization of adsorption for the removal of cadmium from aqueous solution using Turkish coffee grounds, Int. J. Environ. Res., 13 (2019) 861–878.

[49] S.S. Kadhim, R.F. Abbas, S.S. Jaafar, Removal of Cr(VI) from aqueous solution by using polyaniline/polycarbonates nanofibers composite: central composite design, isotherm, and error analysis, Desal. Water Treat., 229 (2021) 343–351.

[50] A.O. Dada, A.P. Olalekan, A.M. Olatunya, O. Dada, Langmuir, Freundlich, Temkin and Dubinin–Radushkevich isotherms studies of equilibrium sorption of Zn^{2+} unto phosphoric acid modified rice husk, IOSR J. Appl. Chem., 3 (2012) 38–45.

[51] E.C. Lima, A.A. Gomes, H.N. Tran, Comparison of the nonlinear and linear forms of the van't Hoff equation for calculation of adsorption thermodynamic parameters ($\Delta S°$ and $\Delta H°$), J. Mol. Liq., 311 (2020) 113315, doi: 10.1016/j.molliq.2020.113315.

[52] Sumanjit, S. Rani, R.K. Mahajan, Equilibrium, kinetics and thermodynamic parameters for adsorptive removal of dye Basic Blue 9 by ground nut shells and *Eichhornia*, Arabian J. Chem., 9 (2016) S1464–S1477.

[53] E.D. Revellame, D.L. Fortela, W. Sharp, R. Hernandez, M.E. Zappi, Adsorption kinetic modeling using pseudo-first-order and pseudo-second-order rate laws: a review, Cleaner Eng. Technol., 1 (2020) 100032, doi: 10.1016/j.clet.2020.100032.

[54] M.A. Hubbe, S. Azizian, S. Douven, Implications of apparent pseudo-second-order adsorption kinetics onto cellulosic materials: a review, BioResources, 14 (2019) 7582–7626.

[55] M.M. Merza, R.A. Al-Bayati, M.J.M. Hassan, Investigation the adsorption properties of the Iraqi siliceous rocks composite towards some heavy metal, Egypt. J. Chem., 64 (2021) 6203–6212.

[56] D. Maiti, S. Mukhopadhyay, P.S. Devi, Evaluation of mechanism on selective, rapid, and superior adsorption of Congo red by reusable mesoporous α-Fe_2O_3 nanorods, ACS Sustainable Chem. Eng., 5 (2017) 11255–11267.

[57] S. Ranjbari, A. Ayati, B. Tanhaei, A. Al-Othman, F. Karimi, The surfactant-ionic liquid bi-functionalization of chitosan beads for their adsorption performance improvement toward Tartrazine, Environ. Res., 204 (2022) 111961, doi: 10.1016/j.envres.2021.111961.

[58] S. Perveen, R. Nadeem, F. Nosheen, M.I. Asjad, J. Awrejcewicz, T. Anwar, Biochar-mediated zirconium ferrite nanocomposites for tartrazine dye removal from textile wastewater, Nanomaterials, 12 (2022) 2828, doi: 10.3390/nano12162828.

[59] R.K. Gautam, S. Banerjee, M.A. Sanroman, M.C. Chattopadhyaya, Synthesis of copper coordinated dithiooxamide metal organic framework and its performance assessment in the adsorptive removal of tartrazine from water, J. Environ. Chem. Eng., 5 (2017) 328–340.

[60] S. Banerjee, M.C. Chattopadhyaya, Adsorption characteristics for the removal of a toxic dye, tartrazine from aqueous solutions by a low-cost agricultural by-product, Arabian J. Chem., 10 (2017) S1629–S1638.

[61] J. Goscianska, R. Pietrzak, Removal of tartrazine from aqueous solution by carbon nanotubes decorated with silver nanoparticles, Catal. Today, 249 (2015) 259–264.

[62] H.O. Chukwuemeka-Okorie, F.K. Ekuma, K.G. Akpomie, J.C. Nnaji, A.G. Okereafor, Adsorption of tartrazine and sunset yellow anionic dyes onto activated carbon derived from cassava sievate biomass, Appl. Water Sci., 11 (2021) 1–8.